Supplemental Information

SI Notes S1 – Fluid Mechanics Model

As the reservoir rotates at constant angular speed Ω, the fluid escapes through two small circular channels connecting the bottom of the reservoir to the exterior. Within the RJS system two flow regimes of interest are expected. First, there is a transition region as the fluid travels from the reservoir and into the channel. This entry flow, similar to flow through circular-circular contractions[49], presents high elongational strain rates. The second type of flow occurs inside the channel as the solution travels outwards before being ejected. Shear is dominant in this second flow regime (Fig. 1c and Fig. S6). When the jet exits the RJS system sudden lateral forces and fiber extension ensue as the fiber travels from the reservoir to the collector[37].

We focus here on the flow inside the RJS system. Extensional flow has been shown to enable protein unfolding and assembly[49-51,76,77]. Polymers in shear flow in contrast experience fluctuations between folded and stretched configuration, so that extremely high shear flows are usually required to unfold globular proteins[52,53,78]. We will first estimate the extensional strain rates in our system's entry flow using Computational Fluid Dynamics (CFD) simulations (Fig. 1c). These values will then be utilized to investigate the propensity of fibronectin (Fn) to unfold using established models of protein dynamics under extensional flow. These models are based on calculations of work (J)[78], force (N)[51] and the dimensionless Deborah number[50] and can then be compared to published literature on Fn properties (SI Notes S2). In a second step, we examine the possibility that shear may also affect Fn's molecular conformation as it travels through the reservoir channel. As performed previously, shear rates were estimated and subsequently interpreted using an established model that calculates the dimensionless Weissenberg number, descriptive of protein unfolding in shear flow[52] (SI Note S3). We conclude by discussing and comparing the different models used in this analysis (SI Note S4).

SI Notes S2 – Models of Fn unfolding in extensional flow (entry flow):

Extensional strain rates calculation in entry flow: CFD simulations allow calculation of the flow profiles. The finite element software COMSOL 5.2a was used. The reservoir has a radius $M = 0.0125$ m and the channel has length $L = 0.0075$ m and radius $R = 200 \times 10^{-6}$ m. Half of the domain was modeled. While the flow inside of the channel is axisymmetric, the entry flow might be affected by the three–dimensional (3D) geometry. Moreover, modeling a smaller domain with only a fraction of the entire fluid domain would require additional assumptions regarding boundary conditions in the vicinity of the channel entry. These considerations were avoided by solving the Navier-Stokes equations in the 3D domain corresponding to half of the reservoir. The geometry is constructed such that the channel centerline is aligned with the x axis and the yz plane is used for the symmetric boundary condition (Fig. S7). The body force due to centrifugal force in this coordinate system is:

$$\boldsymbol{b} = (x\rho\Omega^2, y\rho\Omega^2, 0) \quad \text{(S1)}$$

At the top of the reservoir an inlet boundary condition is specified with zero pressure. An outlet boundary condition is prescribed at the end of the channel also with zero pressure. The plane yz has a symmetry boundary condition. The rest of the walls have no slip conditions. The fluid density is taken as $\rho = 1400$ kg/m^3, and the viscosity as $\mu = 0.1$ Pa·s[38]. A typical rotation speed for the reservoir is $\Omega = 3000$ s^{-1}[1]. The flow was assumed to be laminar. The resulting finite element mesh was composed of tetrahedral elements inside of the domain and quadrilaterals near the boundary. The element size was chosen to be extremely fine leading to a system of 4,297,332 degrees of freedom. Simulations were run until they converged to a relative error of 10^{-7}. The computational cost of each simulation was approximately 1.5 hr in a machine equipped with an Intel Xeon E5-1630 v4 processor consisting of four cores operating at 3.7 GHz, and 16GB RAM.

Supplementary Fig. S7 shows a cross section of the domain on the xz plane passing through the centerline of the channel. The velocity in the majority of the reservoir is close to zero, followed by a region of high

acceleration as the fluid is pushed into the channel. Once the fluid enters the channel, the velocity profile gradually resembles that of a Poiseuille flow. Even though there is a body force that increases away from the center of the reservoir, the speed inside of the channel does not change significantly (Fig. 1c). The velocity u in the x direction has a maximum of 29.6 m/s. The strain rate in the x direction is $\dot{\epsilon} = \partial u/\partial x$ and has a peak value of 0.76×10^5 s^{-1} along the axis of the channel and a maximum of 1.3×10^5 s^{-1} overall.

To verify that the assumption of laminar flow is consistent, the Reynolds number is calculated:

$$Re = \frac{\rho \bar{u} R}{\mu} \tag{S2}$$

Where $\bar{u} = 14.8$m/s is the mean velocity in the channel. In this case, $Re = 41.44$ and laminar flow can be assumed.

1st Model of Fn unfolding in extensional flow: Next the extensional force on Fn due to the strain rate is estimated. Fn can be modeled as a string of 56 globular modules or spherical beads of $a = 2.5$ nm diameter with a contour length of $L_c = 160$ nm[79-82]. The main assumption is that under the influence of the strong extensional flow the molecule begins to unfold just enough such that two spherical sub-clusters are formed separated by a small string of beads[78]. The two spherical sub-clusters consist of n beads and the volume of each sub-cluster is (Fig. S6):

$$v = nv_b = \frac{4}{3}\pi r^3 \tag{S3}$$

Where v_b is the volume of an individual bead and r is the radius of the sub-cluster. The distance between the two sub-clusters can be estimated as $(N - 2n)d$ with d the distance between any two beads. The difference in velocity between the two sub-clusters is:

$$v_2 - v_1 = (N - 2n)d\dot{\epsilon} \tag{S4}$$

The corresponding tension that is created due to the difference in drag force between front and back is:

$$T = T_2 - T_1 = 3\pi\mu\, r\dot{\epsilon}(N - 2n)d \quad \text{(S5)}$$

The value of the tension changes from the initial point in which there is a single bead between the two sub-clusters, to the final fully extended conformation. The integral of the tension as the molecule is completely unfolded yields the total work that will be done on the molecule by the fluid[78]:

$$W = \frac{27}{28}\pi\mu d^2 N^{7/3}\left(\frac{3v_b}{8\pi}\right)^{1/3}\dot{\epsilon} \quad \text{(S6)}$$

For the rotation speed of $\Omega = 3000$ s^{-1} (~28'000 rpm), the calculated work done on a single molecule with this model along the centerline is $W = 0.00235$ fJ and at its maximum is $W = 0.00382$ fJ. Conversely, in previous experiments on Fn nanotextiles[42], the force required to unfold a single molecule was estimated. From the corresponding force-strain relationship the work needed to unfold a single molecule from 15 nm to 60 nm is calculated to be 0.00399 fJ. These values are remarkably close. The analysis suggests that the elongational strain rate produced by the RJS system at rotation speeds of $\Omega = 3000$ s^{-1} would transfer energy to the Fn molecule in sufficient amounts to induce at least partial unfolding.

2nd Model of Fn unfolding in extensional flow: Alternatively, following the analysis of DNA stretching in extensional flow previously described[51], the tension in the stretched polymer should balance the drag forces at equilibrium:

$$\xi\dot{\epsilon}x - F(x) = 0 \quad \text{(S7)}$$

Where ξ is the drag coefficient, x is the length of the polymer in the current configuration, and $F(x)$ is the force in the molecule due to unfolding or stretching. The force can be calculated based on a worm-like chain model for flexible molecules[51]:

$$\frac{F(x)l_p}{k_BT} = \frac{1}{4}\left(1 - \frac{x}{L_c}\right)^{-2} - \frac{1}{4} + \frac{x}{L_c} \quad \text{(S8)}$$

Where l_p is the persistence length. For Fn $l_p = 7$ to 14 nm[80]. The drag coefficient can be approximated using Batchelor's theory of slender bodies in Stokes flow[83]:

$$\xi = \frac{\mu 2\pi L_c}{\ln\left(\frac{L_c}{a}\right)} \quad \text{(S9)}$$

Solving Eq. (S7) the stretch value of $x/L_c = 0.98$ is obtained, and a tension of 494 pN is the one that satisfies equilibrium. This very high force is obtained because the force in the worm-like chain model increases sharply near full extension. According to the literature, forces ranging from 50 to 200 pN have demonstrated unfolding of globular Fn[84], suggesting that the strain rate of 1.3×10^5 s^{-1} should generate enough tension to keep a Fn molecule in a fully extended configuration.

3rd *Model of Fn unfolding in extensional flow:* Finally, the Weissenberg (Wi) number, also called Deborah (De) number, is a nondimensional number that relates elastic and viscous forces or the times scales of relaxation and observation, and is defined as:

$$De = \tau_r \, \dot{\epsilon} \quad (= Wi) \quad \text{(S10)}$$

Where τ_r is the longest relaxation time of the polymer, and can be estimated from the Rouse model as[83]:

$$\tau_r = \frac{\xi \langle r_{ee}^2 \rangle_0}{6\pi^2 k_B T} \quad \text{(S11)}$$

Where ξ is the drag coefficient, $\langle r_{ee}^2 \rangle_0$ is the chain end-to-end distance, k_B is the Boltzmann constant, and T is the temperature. The end-to-end distance can be calculated based on the persistence and contour lengths as:

$$\langle r_{ee}^2 \rangle_0 = 2 l_p L_c \quad \text{(S12)}$$

The relaxation time of Fn is then estimated to be 222 μs. Thus, at the centerline strain rate the Deborah number is $De = 16.6$ and at the maximum strain rate it is $De = 28.9$. It has been determined that a coil-stretch transition occurs at $De = 0.5$, such that for $De > 0.5$ there will be at least some unfolding of the polymer[50]. As the strain rate and, consequently, the Deborah (or Weissenberg) number increases, the polymer is stretched more. For instance, with DNA, which is a flexible chain, a stretch of $x/L_c = 0.82$ is achieved at $De = 4.1$ [50,51]. Thus we expect that De values between 16.6 and 28.9 will be enough to induce Fn unfolding.

Additionally, it must also be noted that the relaxation time and the corresponding critical strain rate are determined for dilute concentrations. Fn has an intrinsic viscosity of 10 mg/L at low ionic strengths and pH 7.4[85]. Thus, the critical concentration to reach a semi-dilute solution is 77 mg/mL[86], whereas the solutions used in this study have a Fn concentrations of 20 mg/mL. Nonetheless, it has been shown that even small deformations of polymer chains in extensional flow fields sharply lower the critical concentration needed for coil-coil interactions between molecules – indicative of semi-dilute regimes[53]. Transitioning to a non-dilute regime can have significant effect on the relaxation time as the molecules aggregate, consequently increasing the local De and Wi values in our flow system. Recent investigations on collagen assembly also showed that solutions in the semi-dilute regime increased the relaxation time by orders of magnitude or, equivalently, reduced the critical strain rate needed for unfolding[77]. In the case of Fn, where fibrillogenesis has even been demonstrated with relatively low strain rates[32,40], this dynamic flow regime should be largely sufficient to prompt molecular unfolding and assembly.

SI Notes S3 – Model of Fn unfolding in shear flow (channel flow):

Shear rates calculation in channel flow: While extensional flow at the channel entry might be the strongest contribution to the initial unfolding of Fn[49], shear flow has been shown to also influence the conformation of flexible polymers[52,53]. Therefore, the shear flow in the channel is now considered (Fig. 1c).

Based on the numerical simulation, even though there is a body force that increases as the fluid moves along the channel, the velocity stays nearly constant. This is consistent with Poiseuille flow through the channel. Let x remain the coordinate along the channel, and r and θ be the radial and circumferential coordinates respectively. Under the assumption of Poiseuille flow, the velocity field is at steady state, is axisymmetric, and only has a nonzero component in the *x* direction that depends solely on the radial coordinate (Fig. S7):

$$u_x(r) = -\frac{1}{4\mu}\left(\frac{\partial p}{\partial x} - b\right)(R^2 - r^2) \tag{S13}$$

where p is the pressure, R is the radius of the orifice, μ denotes dynamic viscosity, and b is a body force. In this coordinate system the centrifugal force is:

$$b = \rho\Omega^2 x \tag{S14}$$

The force of gravity is neglected since for the channel the centripetal acceleration is dominant $g \ll \Omega^2 x$, $x \in [M, M + L]$. To determine the pressure distribution, a quadratic dependence on x is proposed:

$$p(x) = a_1 + a_2 x + a_3 x^2 \tag{S15}$$

The quadratic dependence is needed to satisfy the continuity equation in Poiseuille flow $\partial u_x/\partial x = 0$. Taking the derivative of Equation (S13) with respect to x and setting the expression equal to zero leads to:

$$a_3 = \frac{1}{2}\rho\Omega^2 \quad \text{(S16)}$$

And the velocity profile becomes:

$$u_x(r) = -\frac{1}{4\mu}(a_2)(R^2 - r^2) \quad \text{(S17)}$$

Next, to determine the constant a_2, the pressure drop along the pipe is determined. Inside of the reservoir the fluid is rotating at constant angular speed and therefore it pushes on the inside walls of the reservoir according to the centripetal acceleration $a = \Omega^2 x$. The pressure distribution of the rotating fluid inside the reservoir ignoring gravity is[87]:

$$p = \frac{1}{2}\rho\Omega^2 x^2 \quad \text{(S18)}$$

Therefore, the pressure at the inner wall of the reservoir is:

$$p_{in} = \frac{1}{2}\rho\Omega^2 M^2 = a_1 + a_2 M + \frac{1}{2}\rho\Omega^2 M^2 = p(M) \quad \text{(S19)}$$

The pressure at the outlet of the channel is zero.

$$p_{out} = 0 = a_1 + a_2(M + L) + \frac{1}{2}\rho\Omega^2(M + L)^2 = p(M + L) \quad \text{(S20)}$$

From Eq. (S19) and (S20) the missing constant is determined:

$$a_2 = -\frac{\rho\Omega^2(M+L)^2}{2L} \quad \text{(S21)}$$

And the final expression for the velocity is obtained:

$$u_x(r) = \frac{1}{4\mu}\left(\frac{\rho\Omega^2(M+L)^2}{2L}\right)(R^2 - r^2) \quad \text{(S22)}$$

And the shear rate is readily calculated as

$$\dot{\gamma} = -\frac{\rho\Omega^2(M+L)^2 r}{4\mu L} \quad \text{(S23)}$$

Thus the shear rate depends linearly on the radial coordinate and is quadratic on the angular velocity. This analytical result is in very good agreement with the numerical simulation. For a rotation speed of $\Omega =$

$3000\ s^{-1}$ the maximum velocity using Eq. S22 is 31.9 m/s whereas the simulation predicts 29.5 m/s. Similarly, the shear rate using S23 is $\dot{\gamma} = 3.19 \times 10^5\ s^{-1}$ while the numerical result is $2.9 \times 10^5\ s^{-1}$.

Model for Fn unfolding in shear flow: The conformational changes of polymers in shear flow are governed by the Weissenberg (Wi) number, which is a nondimensional measure that relates elastic and viscous forces:

$$Wi = \dot{\gamma}\ \tau_r \tag{S24}$$

The Weissenbergh (Wi) number at the wall can be calculated using (S18) and gives $Wi = 79.0$. The Wi number is expected to have significant effect on the stretching of the molecules in shear flow[52], measuring the strength of the shear force relative to the relaxation time of the polymer. As the Wi number increases the polymer molecules are expected to present more frequent and larger extensions. When Wi is below 1, the molecules will have Brownian motion and oscillate between coiled and stretched conformations but the effect of the flow remains weak[53]. As Wi increases, oscillation will persist, but it will become more likely to find the molecules in their extended conformation.

For Fn in the rotating reservoir channel, fluctuations of the molecule between different conformational extensions should still be expected. Nonetheless, non-dimensional simulations on wormlike chain models and Kramer bead and rod models for different polymer flexibilities show that the expected mean of relative elongation is in the range of 0.2 to 0.6[53]. Moreover, this behavior is representative of smaller values of Wi, and for the simulations with Wi approaching 80 the elongation achieves an asymptotic limit close to 0.5 for flexible molecules. Considering these Brownian dynamic simulations, we expect that the Wi numbers in the RJS system are thus large enough to further contribute to conformational changes of the Fn molecules in addition to the extensional flow at the channel entry.

SI Notes S4 – Models discussion

Using CFD simulations of the extensional and shear rates (Fig. 1c) as well as established analytical models for predicting protein unfolding under flow (Supplementary Notes S2 and S3), we were able to assess the propensity of Fn to undergo fibrillogenesis in RJS.

The models described above allow comparison of previous work on protein unfolding in different flow regimes with literature on Fn mechanical behavior. However, to elucidate the detailed mechanisms of Fn unfolding and assembly, a more thorough understanding of the spinning process would likely be required. In particular, Brownian dynamic simulations similar to those described previously[53] could provide additional insights into this process. Simpler models can nonetheless provide insight into the physics of the process. The equilibrium model to estimate the force on the molecule disregards the unfolding process[51], yet it supports the idea that an unfolded Fn molecule can be kept in the extended configuration in the RJS' extensional flow field. The work calculation provides a simple characterization of the unfolding process[78] and allows comparison with previous data on Fn force-strain curves[42] also supporting the idea of Fn unfolding in elongational flow. The dimensionless Deborah number or the Weissenberg number enable a wider comparison to theory and experiments done with other flexible polymers such as DNA[50,52] and collagen[77] and further suggests that the strain or shear rates in our system are large enough to induce Fn unfolding.

Finally, we have only considered the flow at the entrance and inside the channel; however conformational changes of Fn may also be induced as the jet exits the channel and is suddenly exposed to large lateral forces. This analysis is beyond the scope of the present work.

SI Methods and Materials

Staining and Imaging: *Haematoxylin and Eosin Staining (H&E).* H&E staining was performed following standard protocols. De-paraffinized sections were stained with Mayers Haematoxylin (Sigma) at room temperature for 3 minutes. Blue staining was performed by rinsing in tap water while differentiation was performed by rinsing in 1% acid ethanol. Samples were counterstained by rinsing with eosin (Sigma) for 30 seconds and dehydrated by sequential washing with 95% ethanol, 100% ethanol and Histo-Clear (National Diagnostics, Atlanta, GA). Slides were covered with cover-slips using DPX (Agar Scientific, UK) and examined by light microscopy using a Olympus VS120 Whole Slide Scanner.

Masson's Trichrome Staining: Masson's Trichrome was performed using Sigma's HT15 Trichrome staining kit according to the manufacturer's instructions (Sigma). Briefly, paraffin embedded tissues were de-paraffinized and rehydrated gradually in graded ethanol. The samples were then fixed in Bouin's solution and incubated in Weigert's Iron Hematoxylin solution. The slides were stained with Biebrich Scarlet-Acid Fuchsin and Aniline Blue, followed by dehydration in ethanol and xylene. The collagen fibers were stained blue, the cell nuclei were stained brown, and keratin and muscle fibers were stained red. Samples were then monitored under a Olympus VS120 Whole Slide Scanner.

Alkaline Phosphatase Staining: Alkaline phosphatase activity was monitored using VectorLab SK-5100 kit (Vector Laboratories, Burlingame, CA) according to manufacturer's instructions. Briefly, frozen tissue sections were rinsed with PBS/0.05% Tween 20 (PBST) shortly and fixed again with 4% formaldehyde for 3-5 min. Samples were then rinsed with PBST and incubated for 20 minutes in the staining mixture composed of two drops of reagents 1, 2 and 3 in 5 ml of Tris 150 mM solution with a pH of 8.3. Samples were then monitored under a Olympus VS120 Whole Slide Scanner.

Immunostaining: Tissue samples were first de-paraffinized and rehydrated gradually in graded ethanol. Heat-induced antigen retrieval was then performed by bathing samples in a solution of Sodium Citrate 0.01M and 0.01% tween at pH=6 in diH_2O at a temperature of 98°C for 20 min, followed by a cooling for

10 min at the bench. Samples were then blocked in NGS (Normal Goat Serum) and 0.3% Tween in PBS for 2 hrs, after which they were incubated for 24 hours at 4°C in primary antibody solutions of PBS with:

- Keratin 5 (mouse) 1: 100 dilution (Invitrogen: MA5-17057)
- Keratin 14 (rabbit) 1: 500 dilution (Biolegend: 905301)
- Keratin 17 (rabbit) 1:100 dilution (Abcam: ab109725)

Samples were then washed (2 x 10 min) and stained with secondary antibodies for 1 hr:

- Alexa Fluor 488 goat anti-rabbit secondary antibody 1:1000 dilution (Invitrogen)
- Alexa Fluor 594 goat anti-mouse secondary antibody 1:1000 dilution (Invitrogen).
- Alexa Fluor 564 goat anti-guinea pig secondary antibody 1:200 dilution (Invitrogen)

After staining, samples were rinsed, mounted on glass slides and imaged under confocal microscopy using a Zeiss LSM 5 LIVE microscope and an Olympus microscope.

Alternatively, samples were blocked for one hour in blocking buffer [PBS (Corning, 21-031-CV) with 5% Normal Donkey Serum and 0.1% Triton-X 100, after which they were incubated for 1 hour in primary antibody solutions of blocking buffer with:

- PPARγ (rabbit) 1:125 dilution (Cell Signaling Tech; C26H12)
- Perilipin (guinea pig) 1:125 dilution (Fitzgerald; 20R-PP004)

Samples were then washed (3 x 3min) with 0.1% Triton-X 100 and stained with secondary antibodies for 30 min:

- Alexa Fluor 488 donkey anti-rabbit secondary antibody 1:1000 dilution (Life Technologies)
- Alexa Fluor 594 goat anti-guinea pig secondary antibody 1:1000 dilution (Life Technologies).

Tissues were then counterstained with 20 µg/mL Hoechst 33342 (Life Technologies, H1399) in PBS for five minutes, washed and mounted.

Fn immunostaining: Fn fiber staining was performed by likewise de-paraffinizing and re-hydrating tissue samples at day 6 post-treatment. Samples were then incubated in a PBS solution of:

- Anti-Fn antibody (rabbit) 1: 200 dilution (Abcam: MA5-17057)

Samples were then washed (3 x 10min) and stained in a PBS solution for one hour of DAPI (1:200) and:

- Alexa Fluor 546 goat anti-rabbit secondary antibody 1:200 dilution (Invitrogen)

Samples were then washed and mounted for imaging.

References

1 Sen, C. K. *et al.* Human skin wounds: a major and snowballing threat to public health and the economy. *Wound Repair Regen* **17**, 763-771 (2009).

2 Gurtner, G. C., Werner, S., Barrandon, Y. & Longaker, M. T. Wound repair and regeneration. *Nature* **453**, 314-321 (2008).

3 Martin, P. Wound healing--aiming for perfect skin regeneration. *Science* **276**, 75-81 (1997).

4 Corr, D. T., Gallant-Behm, C. L., Shrive, N. G. & Hart, D. A. Biomechanical behavior of scar tissue and uninjured skin in a porcine model. *Wound Repair Regen* **17**, 250-259 (2009).

5 Tomasek, J. J., Gabbiani, G., Hinz, B., Chaponnier, C. & Brown, R. A. Myofibroblasts and mechano-regulation of connective tissue remodelling. *Nat Rev Mol Cell Biol* **3**, 349-363 (2002).

6 Lee, K. & Hubbell, J. A. Tissue, cell and engineering. *Curr Opin Biotechnol* **24**, 827-829 (2013).

7 Lutolf, M. P. & Hubbell, J. A. Synthetic biomaterials as instructive extracellular microenvironments for morphogenesis in tissue engineering. *Nature Biotechnol.* **23**, 47-55 (2005).

8 Guvendiren, M. & Burdick, J. A. Engineering synthetic hydrogel microenvironments to instruct stem cells. *Curr Opin Biotechnol* **24**, 841-846 (2013).

9 Lutolf, M. P. *et al.* Synthetic matrix metalloproteinase-sensitive hydrogels for the conduction of tissue regeneration: engineering cell-invasion characteristics. *Proc Natl Acad Sci U S A* **100**, 5413-5418 (2003).

10 Griffin, D. R., Weaver, W. M., Scumpia, P. O., Di Carlo, D. & Segura, T. Accelerated wound healing by injectable microporous gel scaffolds assembled from annealed building blocks. *Nature materials* **14**, 737-744, doi:10.1038/nmat4294 (2015).

11 Place, E. S., Evans, N. D. & Stevens, M. M. Complexity in biomaterials for tissue engineering. *Nat Mater* **8**, 457-470 (2009).

12 Murphy, P. S. & Evans, G. R. Advances in wound healing: a review of current wound healing products. *Plast Surg Int* **190436**, 22 (2012).

13 Banyard, D. A., Bourgeois, J. M., Widgerow, A. D. & Evans, G. R. Regenerative biomaterials: a review. *Plast Reconstr Surg* **135**, 1740-1748 (2015).

14 Zhong, S. P., Zhang, Y. Z. & Lim, C. T. Tissue scaffolds for skin wound healing and dermal reconstruction. *Wiley Interdiscip Rev Nanomed Nanobiotechnol* **2**, 510-525 (2010).

15 Rowlatt, U. Intrauterine wound healing in a 20 week human fetus. *Virchows Arch A Pathol Anat Histol* **381**, 353-361 (1979).

16 Coolen, N. A., Schouten, K., Middelkoop, E. & Ulrich, M. M. W. *Comparison between human fetal and adult skin*. (Arch Dermatol Res. 2010 Jan;302(1):47-55. Epub 2009 Aug 23 doi:10.1007/s00403-009-0989-8.).

17 Longaker, M. T. *et al.* Studies in fetal wound healing: III. Early deposition of fibronectin distinguishes fetal from adult wound healing. *J Pediatr Surg* **24**, 799-805 (1989).

18 Larson, B. J., Longaker, M. T. & Lorenz, H. P. Scarless fetal wound healing: a basic science review. *Plast Reconstr Surg* **126**, 1172-1180 (2010).

19 Namazi, M. R., Fallahzadeh, M. K. & Schwartz, R. A. Strategies for prevention of scars: what can we learn from fetal skin? *Int J Dermatol* **50**, 85-93 (2011).

20 Ji, Y. *et al.* Electrospun three-dimensional hyaluronic acid nanofibrous scaffolds. *Biomaterials* **27**, 3782-3792 (2006).

21 Ghosh, K., Ren, X. D., Shu, X. Z., Prestwich, G. D. & Clark, R. A. Fibronectin functional domains coupled to hyaluronan stimulate adult human dermal fibroblast responses critical for wound healing. *Tissue Eng* **12**, 601-613 (2006).

22 Roy, D. C., Mooney, N. A., Raeman, C. H., Dalecki, D. & Hocking, D. C. Fibronectin matrix mimetics promote full-thickness wound repair in diabetic mice. *Tissue engineering. Part A* **19**, 2517-2526, doi:10.1089/ten.TEA.2013.0024 (2013).
23 Martino, M. M. *et al.* Engineering the growth factor microenvironment with fibronectin domains to promote wound and bone tissue healing. *Sci Transl Med* **3**, 3002614 (2011).
24 Qiu, Z., Kwon, A. H. & Kamiyama, Y. Effects of plasma fibronectin on the healing of full-thickness skin wounds in streptozotocin-induced diabetic rats. *J Surg Res* **138**, 64-70 (2007).
25 Hamed, S. *et al.* Fibronectin potentiates topical erythropoietin-induced wound repair in diabetic mice. *J Invest Dermatol* **131**, 1365-1374 (2011).
26 To, W. S. & Midwood, K. S. Plasma and cellular fibronectin: distinct and independent functions during tissue repair. *Fibrogenesis Tissue Repair* **4**, 1755-1536 (2011).
27 Clark, R. A., Ghosh, K. & Tonnesen, M. G. Tissue engineering for cutaneous wounds. *J Invest Dermatol* **127**, 1018-1029 (2007).
28 Williams, E. C., Janmey, P. A., Johnson, R. B. & Mosher, D. F. Fibronectin. Effect of disulfide bond reduction on its physical and functional properties. *J Biol Chem* **258**, 5911-5914 (1983).
29 Sakai, K., Fujii, T. & Hayashi, T. Cell-free formation of disulfide-bonded multimer from isolated plasma fibronectin in the presence of a low concentration of SH reagent under a physiological condition. *J Biochem* **115**, 415-421 (1994).
30 Ejim, O. S., Blunn, G. W. & Brown, R. A. Production of artificial-orientated mats and strands from plasma fibronectin: a morphological study. *Biomaterials* **14**, 743-748 (1993).
31 Smith, M. L. *et al.* Force-induced unfolding of fibronectin in the extracellular matrix of living cells. *PLoS Biol* **5** (2007).
32 Raoufi, M. *et al.* Nanopore Diameters Tune Strain in Extruded Fibronectin Fibers. *Nano Lett* **15**, 6357-6364, doi:10.1021/acs.nanolett.5b01356 (2015).
33 Reneker, D. H. & Yarin, A. L. Electrospinning jets and polymer nanofibers. *Polymer* **49**, 2387-2425, doi:http://dx.doi.org/10.1016/j.polymer.2008.02.002 (2008).
34 Huang, Z.-M., Zhang, Y.-Z., Kotaki, M. & Ramakrishna, S. A review on polymer nanofibers by electrospinning and their applications in nanocomposites. *Composites science and technology* **63**, 2223-2253 (2003).
35 Badrossamay, M. R., McIlwee, H. A., Goss, J. A. & Parker, K. K. Nanofiber assembly by rotary jet-spinning. *Nano Lett* **10**, 2257-2261 (2010).
36 Badrossamay, M. R. *et al.* Engineering hybrid polymer-protein super-aligned nanofibers via rotary jet spinning. *Biomaterials* **35**, 3188-3197 (2014).
37 Mellado, P. *et al.* A simple model for nanofiber formation by rotary jet-spinning. *Applied Physics Letters* **99**, 203107, doi:10.1063/1.3662015 (2011).
38 Golecki, H. M. *et al.* Effect of solvent evaporation on fiber morphology in rotary jet spinning. *Langmuir : the ACS journal of surfaces and colloids* **30**, 13369-13374, doi:10.1021/la5023104 (2014).
39 Baneyx, G., Baugh, L. & Vogel, V. Coexisting conformations of fibronectin in cell culture imaged using fluorescence resonance energy transfer. *Proc Natl Acad Sci U S A* **98**, 14464-14468 (2001).
40 Little, W. C., Smith, M. L., Ebneter, U. & Vogel, V. Assay to mechanically tune and optically probe fibrillar fibronectin conformations from fully relaxed to breakage. *Matrix Biol* **27**, 451-461 (2008).
41 Vogel, V. Mechanotransduction involving multimodular proteins: Converting force into biochemical signals. *Annual Review of Biophysics and Biomolecular Structure* **35**, 459-488, doi:10.1146/annurev.biophys.35.040405.102013 (2006).
42 Deravi, L. F. *et al.* Differential contributions of conformation extension and domain unfolding to properties of fibronectin nanotextiles. *Nano Lett* **12**, 5587-5592 (2012).

43 Ito, M. Stem cells in the hair follicle bulge contribute to wound repair but not to homeostasis of the epidermis. *Nature Med.* **11**, 1351-1354 (2005).

44 Ito, M. Wnt-dependent de novo hair follicle regeneration in adult mouse skin after wounding. *Nature* **447**, 316-320 (2007).

45 Sullivan, T. P., Eaglstein, W. H., Davis, S. C. & Mertz, P. The pig as a model for human wound healing. *Wound Repair Regen* **9**, 66-76 (2001).

46 Rezakhaniha, R. *et al.* Experimental investigation of collagen waviness and orientation in the arterial adventitia using confocal laser scanning microscopy. *Biomechanics and modeling in mechanobiology* **11**, 461-473, doi:10.1007/s10237-011-0325-z (2012).

47 Parlee, S. D., Lentz, S. I., Mori, H. & MacDougald, O. A. Quantifying size and number of adipocytes in adipose tissue. *Methods in enzymology* **537**, 93-122, doi:10.1016/b978-0-12-411619-1.00006-9 (2014).

48 Emmert, M. Y. *et al.* Safety and efficacy of cardiopoietic stem cells in the treatment of post-infarction left-ventricular dysfunction - From cardioprotection to functional repair in a translational pig infarction model. *Biomaterials* **122**, 48-62, doi:10.1016/j.biomaterials.2016.11.029 (2017).

49 Dobson, J. *et al.* Inducing protein aggregation by extensional flow. *Proc Natl Acad Sci U S A* **114**, 4673-4678, doi:10.1073/pnas.1702724114 (2017).

50 Perkins, T. T., Smith, D. E. & Chu, S. Single Polymer Dynamics in an Elongational Flow. *Science* **276**, 2016 (1997).

51 Larson, R. G., Hu, H., Smith, D. E., & Chu, S. Brownian dynamics simulations of a DNA molecule in an extensional flow field. . *Journal of Rheology* **43**, 267-304 (1999).

52 Smith, D. E., Babcock, H. P. & Chu, S. Single-polymer dynamics in steady shear flow. *Science* **283**, 1724-1727 (1999).

53 Hur, J. S., Shaqfeh, E. S. G. & Larson, R. G. Brownian dynamics simulations of single DNA molecules in shear flow. *Journal of Rheology* **44**, 713-742, doi:10.1122/1.551115 (2000).

54 Ahn, S. *et al.* Self-organizing large-scale extracellular-matrix protein networks. *Adv Mater* **27**, 2838-2845 (2015).

55 Verhaegen, P. D. *et al.* Differences in collagen architecture between keloid, hypertrophic scar, normotrophic scar, and normal skin: An objective histopathological analysis. *Wound repair and regeneration : official publication of the Wound Healing Society [and] the European Tissue Repair Society* **17**, 649-656, doi:10.1111/j.1524-475X.2009.00533.x (2009).

56 Capulli, A. K. *et al.* JetValve: Rapid manufacturing of biohybrid scaffolds for biomimetic heart valve replacement. *Biomaterials* **133**, 229-241, doi:10.1016/j.biomaterials.2017.04.033 (2017).

57 Yang, S. W., Geng, Z. J., Ma, K., Sun, X. Y. & Fu, X. B. Comparison of the histological morphology between normal skin and scar tissue. *Journal of Huazhong University of Science and Technology. Medical sciences = Hua zhong ke ji da xue xue bao. Yi xue Ying De wen ban = Huazhong keji daxue xuebao. Yixue Yingdewen ban* **36**, 265-269, doi:10.1007/s11596-016-1578-7 (2016).

58 Tandara, A. A. & Mustoe, T. A. The role of the epidermis in the control of scarring: evidence for mechanism of action for silicone gel. *Journal of plastic, reconstructive & aesthetic surgery : JPRAS* **61**, 1219-1225, doi:10.1016/j.bjps.2008.03.022 (2008).

59 Ferguson, M. W. & O'Kane, S. Scar-free healing: from embryonic mechanisms to adult therapeutic intervention. *Philosophical transactions of the Royal Society of London. Series B, Biological sciences* **359**, 839-850, doi:10.1098/rstb.2004.1475 (2004).

60 Xue, M. & Jackson, C. J. Extracellular Matrix Reorganization During Wound Healing and Its Impact on Abnormal Scarring. *Advances in wound care* **4**, 119-136, doi:10.1089/wound.2013.0485 (2015).

61 Wang, X., Ge, J., Tredget, E. E. & Wu, Y. The mouse excisional wound splinting model, including applications for stem cell transplantation. *Nat Protoc* **8**, 302-309 (2013).
62 Reynolds, A. J., Lawrence, C., Cserhalmi-Friedman, P. B., Christiano, A. M. & Jahoda, C. A. Trans-gender induction of hair follicles. *Nature* **402**, 33-34 (1999).
63 Oshima, H., Rochat, A., Kedzia, C., Kobayashi, K. & Barrandon, Y. Morphogenesis and renewal of hair follicles from adult multipotent stem cells. *Cell* **104**, 233-245 (2001).
64 Blanpain, C. & Fuchs, E. Epidermal homeostasis: a balancing act of stem cells in the skin. *Nat Rev Mol Cell Biol* **10**, 207-217 (2009).
65 Festa, E. *et al.* Adipocyte lineage cells contribute to the skin stem cell niche to drive hair cycling. *Cell* **146**, 761-771 (2011).
66 Plikus, M. V. *et al.* Regeneration of fat cells from myofibroblasts during wound healing. *Science (New York, N.Y.)* **355**, 748-752, doi:10.1126/science.aai8792 (2017).
67 Sood, A., Granick, M. S. & Tomaselli, N. L. *Wound Dressings and Comparative Effectiveness Data*. (Adv Wound Care (New Rochelle). 2014 Aug 1;3(8):511-529.).
68 Sheehy, S. P. *et al.* Quality metrics for stem cell-derived cardiac myocytes. *Stem Cell Reports* **2**, 282-294 (2014).
69 Varkey, M., Ding, J. & Tredget, E. E. Advances in Skin Substitutes-Potential of Tissue Engineered Skin for Facilitating Anti-Fibrotic Healing. *Journal of functional biomaterials* **6**, 547-563, doi:10.3390/jfb6030547 (2015).
70 Metcalfe, A. D. & Ferguson, M. W. Tissue engineering of replacement skin: the crossroads of biomaterials, wound healing, embryonic development, stem cells and regeneration. *Journal of the Royal Society, Interface* **4**, 413-437, doi:10.1098/rsif.2006.0179 (2007).
71 MacNeil, S. Progress and opportunities for tissue-engineered skin. *Nature* **445**, 874-880 (2007).
72 Sun, G. *et al.* Dextran hydrogel scaffolds enhance angiogenic responses and promote complete skin regeneration during burn wound healing. *Proceedings of the National Academy of Sciences of the United States of America* **108**, 20976-20981, doi:10.1073/pnas.1115973108 (2011).
73 Johnson, M. B. *et al.* Topical Fibronectin Improves Wound Healing of Irradiated Skin. *Scientific reports* **7**, 3876, doi:10.1038/s41598-017-03614-y (2017).
74 Martino, M. M. *et al.* Engineering the growth factor microenvironment with fibronectin domains to promote wound and bone tissue healing. *Science translational medicine* **3**, 100ra189, doi:10.1126/scitranslmed.3002614 (2011).
75 Kwon, A. H., Qiu, Z. & Hirao, Y. Topical application of plasma fibronectin in full-thickness skin wound healing in rats. *Experimental biology and medicine (Maywood, N.J.)* **232**, 935-941 (2007).

Supplementary Information References

76 Sing, C. E. & Alexander-Katz, A. Elongational Flow Induces the Unfolding of von Willebrand Factor at Physiological Flow Rates. *Biophysical Journal* **98**, L35-37, doi:10.1016/j.bpj.2010.01.032 (2010).

77 Paten, J. A. *et al.* Flow-Induced Crystallization of Collagen: A Potentially Critical Mechanism in Early Tissue Formation. *ACS nano* **10**, 5027-5040, doi:10.1021/acsnano.5b07756 (2016).

78 Jaspe, J. & Hagen, S. J. Do Protein Molecules Unfold in a Simple Shear Flow? *Biophysical Journal* **91**, 3415-3424, doi:10.1529/biophysj.106.089367 (2006).

79 Erickson, H. P. & Carrell, N. A. Fibronectin in extended and compact conformations. Electron microscopy and sedimentation analysis. *J Biol Chem* **258**, 14539-14544 (1983).

80 Pelta, J., Berry, H., Fadda, G. C., Pauthe, E. & Lairez, D. Statistical conformation of human plasma fibronectin. *Biochemistry* **39**, 5146-5154 (2000).

81 Feinberg, A. W. & Parker, K. K. Surface-initiated assembly of protein nanofabrics. *Nano Lett* **10**, 2184-2191, doi:10.1021/nl100998p (2010).

82 Bradshaw M , J. & Smith M , L. Contribution of Unfolding and Intermolecular Architecture to Fibronectin Fiber Extensibility. *Biophysical Journal* **101**, 1740-1748, doi:10.1016/j.bpj.2011.08.029 (2011).

83 Saeidi, N., Sander, E. A. & Ruberti, J. W. Dynamic shear-influenced collagen self-assembly. *Biomaterials* **30**, 6581-6592, doi:http://doi.org/10.1016/j.biomaterials.2009.07.070 (2009).

84 Erickson, H. P. Protein unfolding under isometric tension-what force can integrins generate, and can it unfold FNIII domains? *Current opinion in structural biology* **42**, 98-105, doi:10.1016/j.sbi.2016.12.002 (2017).

85 Williams, E. C., Janmey, P. A., Ferry, J. D. & Mosher, D. F. Conformational states of fibronectin. Effects of pH, ionic strength, and collagen binding. *J Biol Chem* **257**, 14973-14978 (1982).

86 C. Clasen, J. P. P., and W.-M. Kulicke. How dilute are dilute solutions in extensional flows? *Journal of Rheology* **50** (2006).

87 Lubarda, V. A. The shape of a liquid surface in a uniformly rotating cylinder in the presence of surface tension. *Acta Mechanica* **224**, 1365-1382, doi:10.1007/s00707-013-0813-6 (2013).

Supplementary Figures

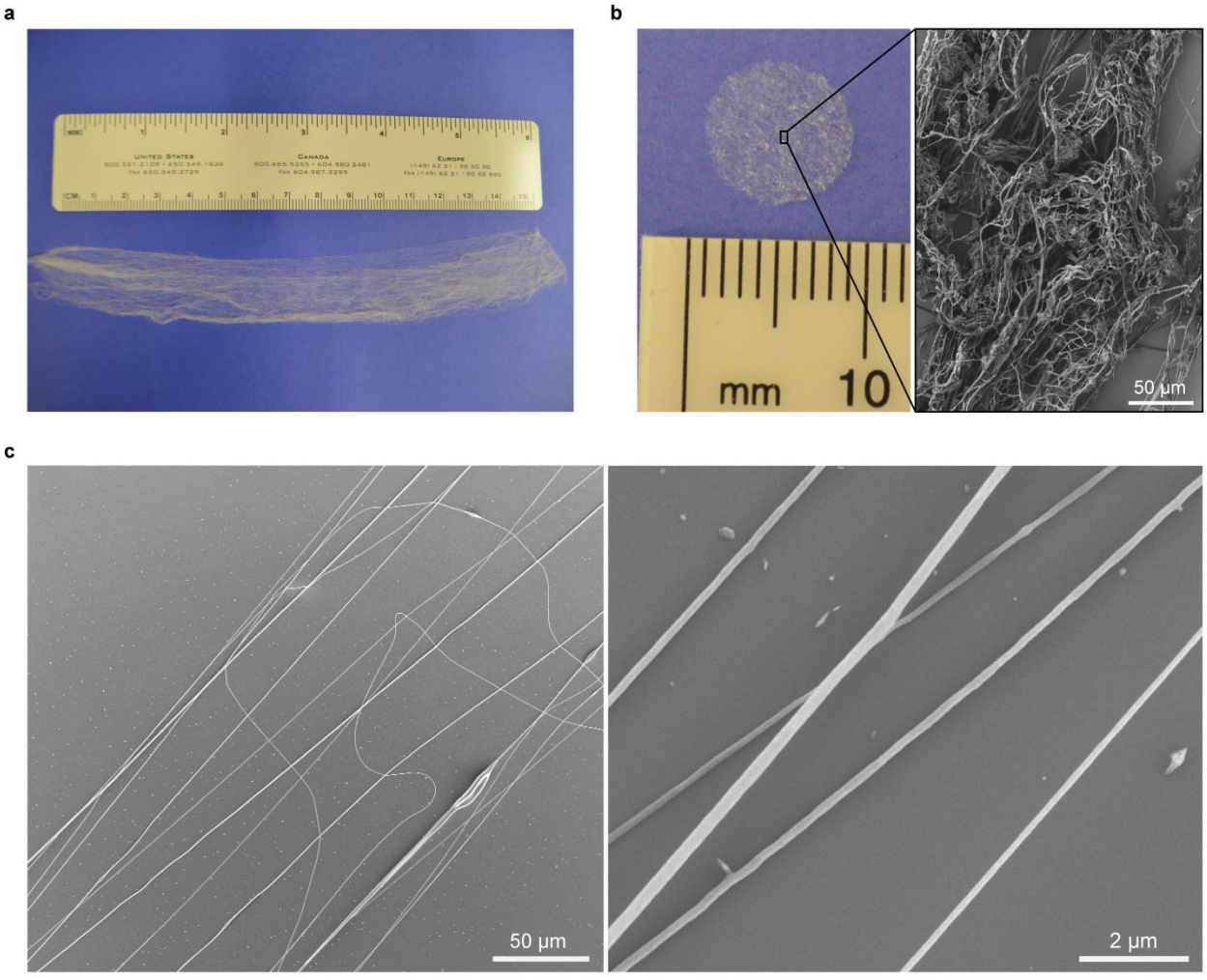

Fig. S1 Fn scaffolds fabricated using the RJS. (**a**) Photograph of a sheet of Fn fibers (approx. 100-200µm in thickness) spun at ~30,000 rpm using the RJS, collected on a rotating mandrel and unrolled post-spinning. (**b**) Fn nanofibers are then cut into 8mm discs with a biopsy punch and used for imaging (right panel shows SEM image) or used subsequently for *in vivo* studies. (**c**) SEM images show fabrication of intact and smooth Fn nanofibers with an average diameter of 457nm ±138.

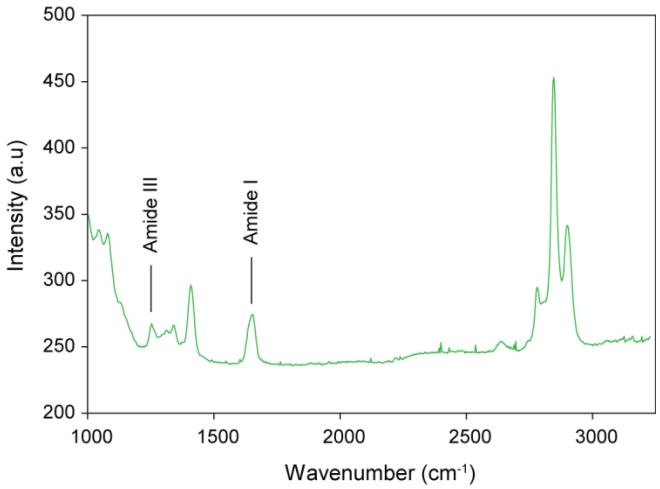

Fig. S2 Chemical structure analysis of Fn fibers by Raman spectroscopy. Raman spectrum shows intact secondary structure of Fn fibers with the presence of Amide 1 (1649cm^{-1}) and Amide III (1249cm^{-1}) peaks. Absence of Amide II peak suggest that tertiary structures are in partially folded states.

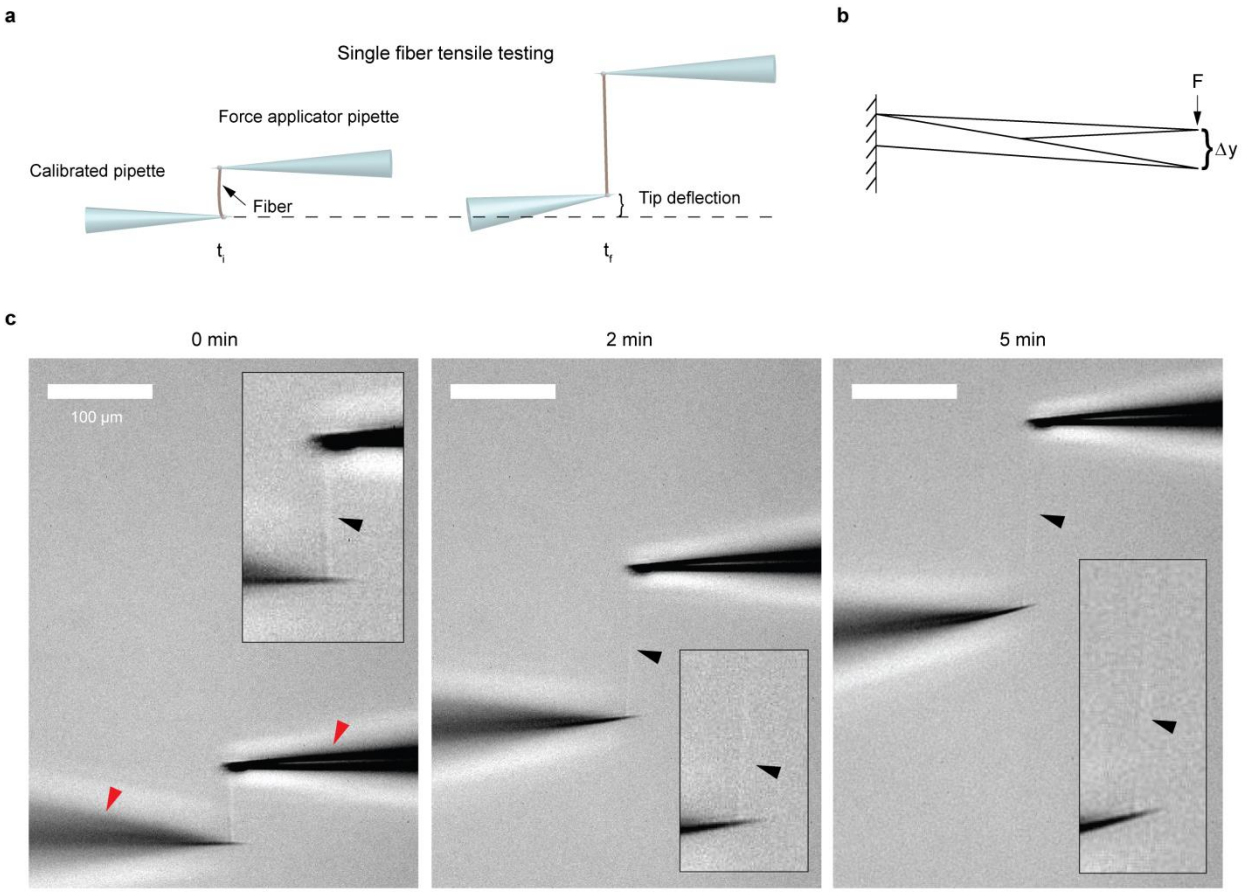

Fig. S3 Single fiber µ-pipette uniaxial tensile testing. (**a**), The testing setup consists of one calibrated pipette and one force applicator pipette to which a fiber is adhered by a droplet of epoxy. Tip deflection is measured as the fiber is pulled. (**b**) Force is measured based on calculated beam stiffness. A known force (F) will deflect the pipette tip a known distance (Δy). (**c**) Representative differential interference contrast (DIC) images of a single Fn nanofiber (black arrowheads) attached between two µ-pipettes (red arrowheads). DIC images represent different time points (0, 2 and 5min) during uniaxial tensile testing (300% strain). DIC images show tip deflection as described in (**a-b**).

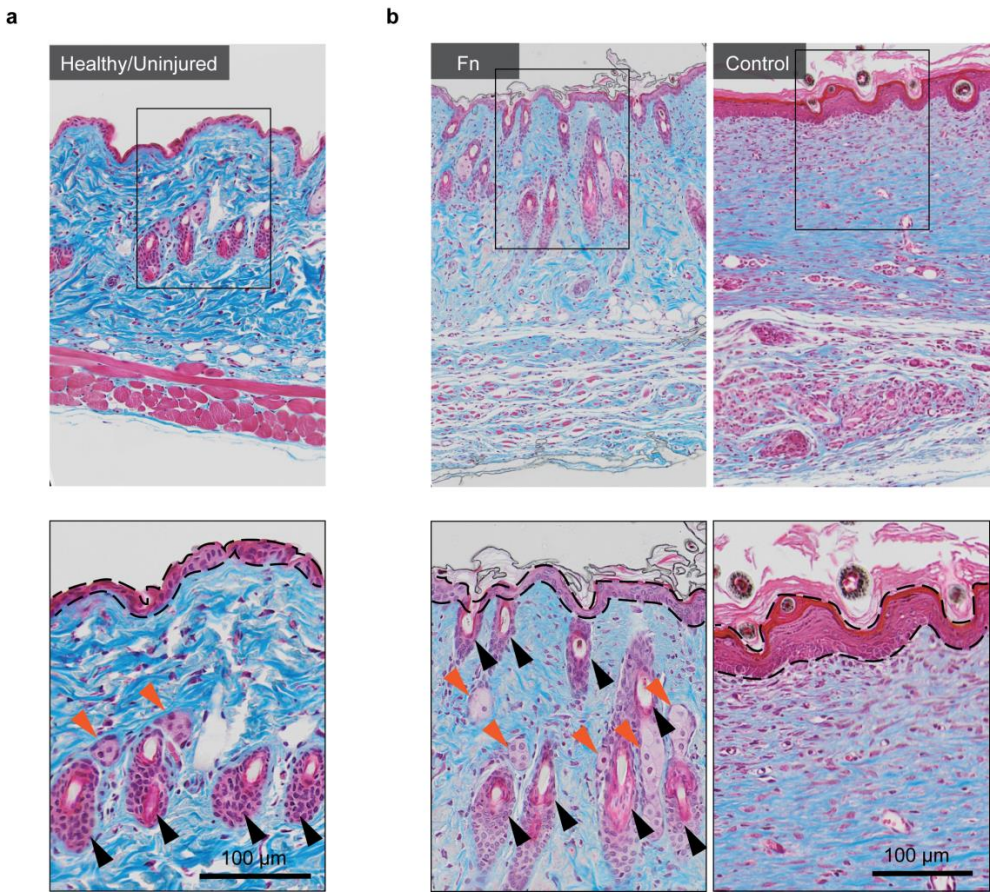

Fig. S4 Epidermal thickness measurements and skin appendage density analysis description. To determine if treated wounds had recovered original healthy epidermal structure, epidermal thicknesses of the different treated tissues were measured 20 days post wounding and compared to healthy uninjured tissue. To verify recovery of dermal architecture, density of hair follicles and sebaceous glands in the treated-wounds were calculated using the same tissue sections. (**a**) Masson's trichrome staining image of unwounded healthy tissue with black dashed lines delimiting the epidermal layer in the skin tissue. Black and orange arrowheads mark the presence of hair follicles and sebaceous glands, respectively. (**b**) Representative images of wound centers 20 days post injury reveal epidermal thickness recovery for Fn treatments whereas the control remains thicker. Arrowheads demonstrate high abundance of hair follicles and sebaceous glands in the Fn treatment. The control condition was void of any skin appendages at the center of the wounds.

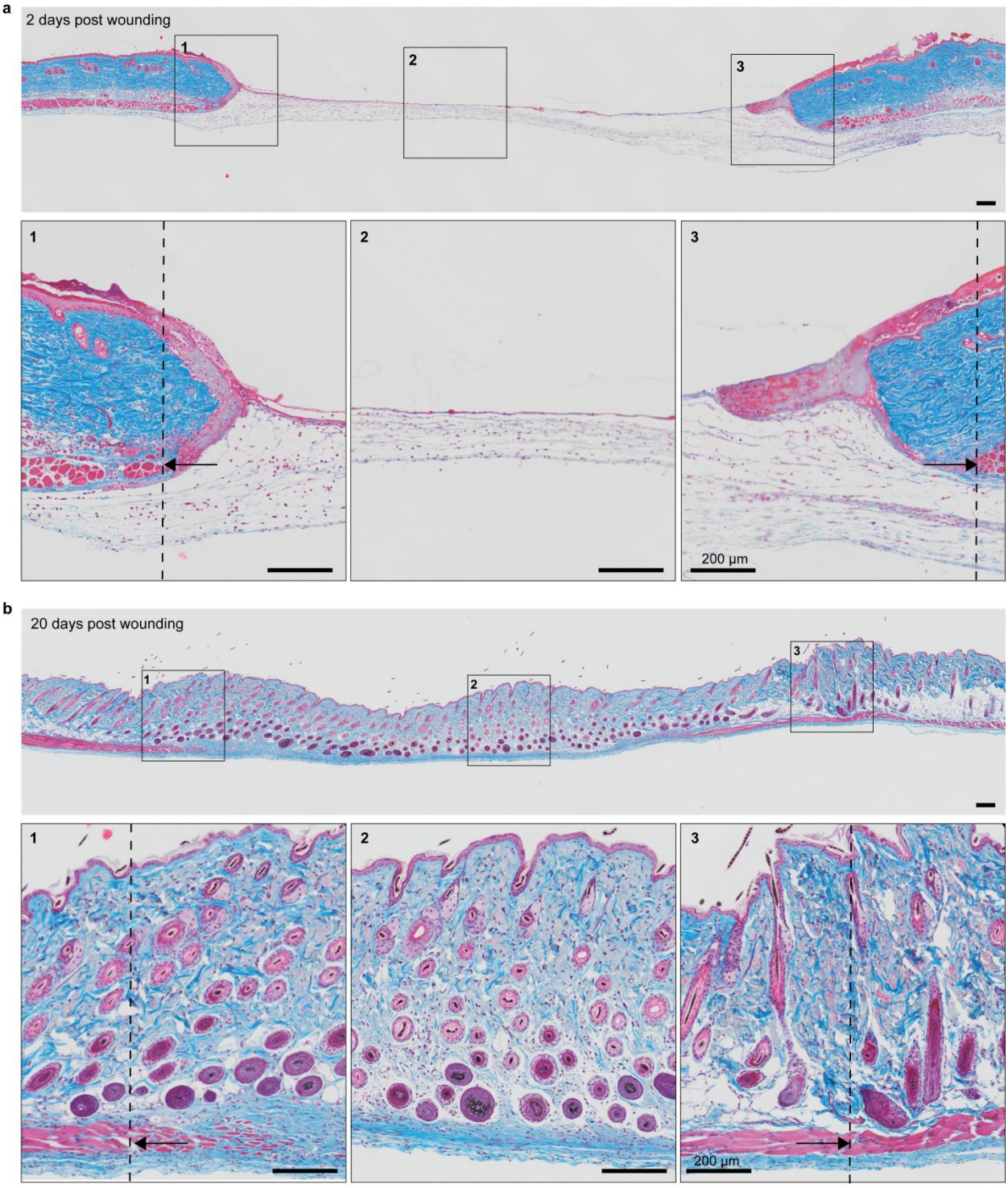

Fig. S5 Establishing wound edges for consistent measurements. To perform accurate and consistent measurements between our different treatment samples, wound edges were defined using the positions of the sectioned panniculus carnosus muscle tissue (black arrows). (**a**) Masson's trichrome images of a non-treated full-thickness wound two days post injury, demonstrating removal of the epidermis, the dermis, hypodermis and the underlying muscle tissue. Insets display position of original wound edges with position of muscle tissue. (**b**) Images of a full-thickness wound 20 days post injury treated with a Fn nanofiber wound dressing. Insets display original position of wound edges.

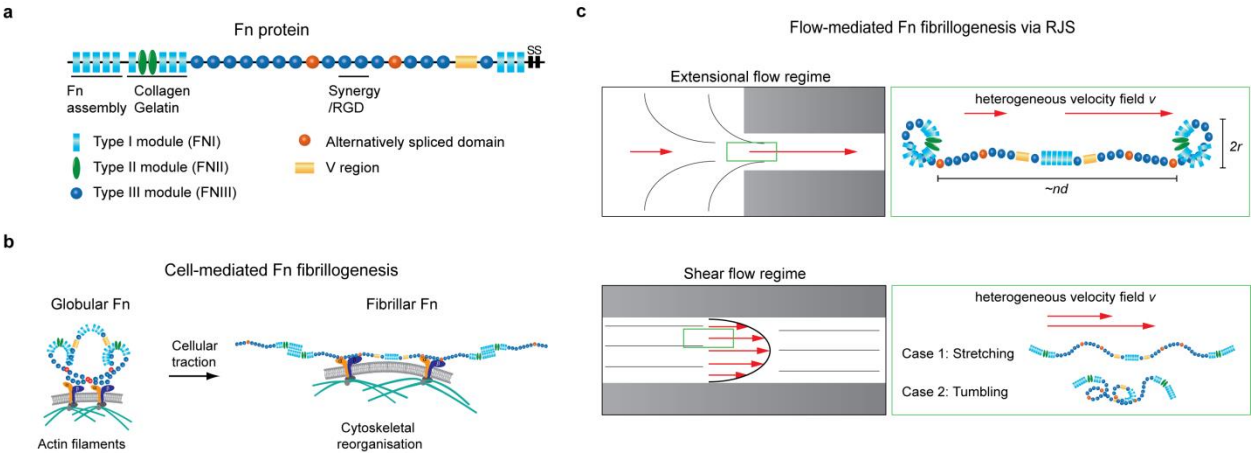

Fig. S6 Cell-mediated Fn unfolding and a theoretical model of Fn unfolding in the RJS system. (**a**) Schematic of the Fn molecular structure with relevant domains labeled. Of specific interest are the FNI_{1-5} domains responsible for Fn assembly during fibrillogenesis, FNIII domains with embedded beta-sheet structures providing mechanical elasticity and the $FNIII_{9-10}$ RGD and synergy sites necessary for cellular adhesion. (**b**) Mechanism of Fn fibrillogenesis *in vivo*. Globular Fn binds to cells via integrin-binding sites, inducing actin cytoskeletal reorganization and cell contractility. This in turn enables unfolding of the Fn molecule, exposing N-terminal Fn-Fn binding sites (FNI_{1-5}) and generating polymerization of Fn into insoluble fibrils. (**c**) Mechanism of flow-mediated Fn fibrillogenesis studied at the entry flow, where high extensional strain is experienced and the channel flow, where high shear is experienced. Insets show Fn molecules undergo stretching due to extensional strain (top) or shear (bottom) rates. (Top) An Fn molecule under a heterogeneous velocity field v can be modeled as a string of N modules, with a diameter a and separated by a center-to-center distance d, while the clusters have a radius r. (Bottom) Because of the heterogeneous velocity field perpendicular to the channel flow, the Fn molecule may either continue to stretch or become unstable and tumble.

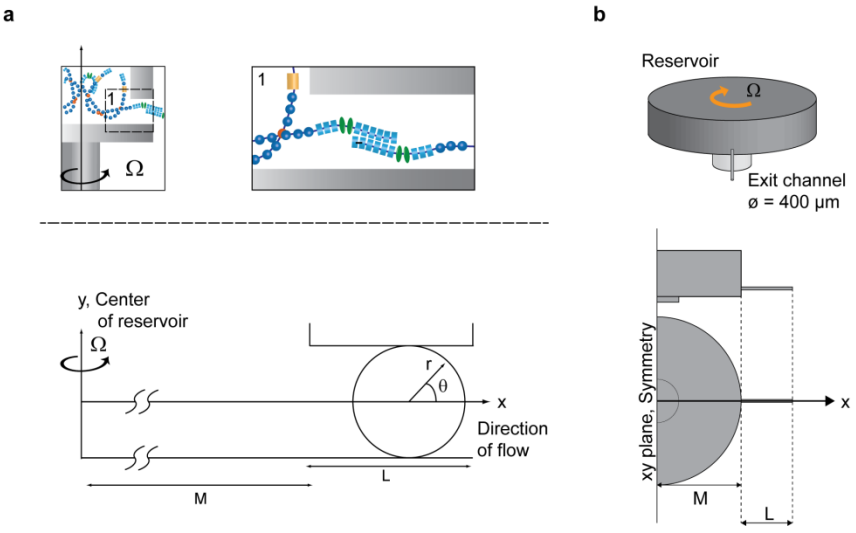

Fig. S7 Parameters for the CFD simulations. (**a**) Schematic representation of the RJS reservoir and orifice (top, and inset 1). The diagram below illustrates the reservoir section with the parameters relevant to the analytical model and CFD simulations. (**b**) Geometries of the Fn solution in the reservoir and the channel for the CFD simulations are constructed such that the centerline is aligned with the x axis and the yz plane for the symmetric boundary condition.

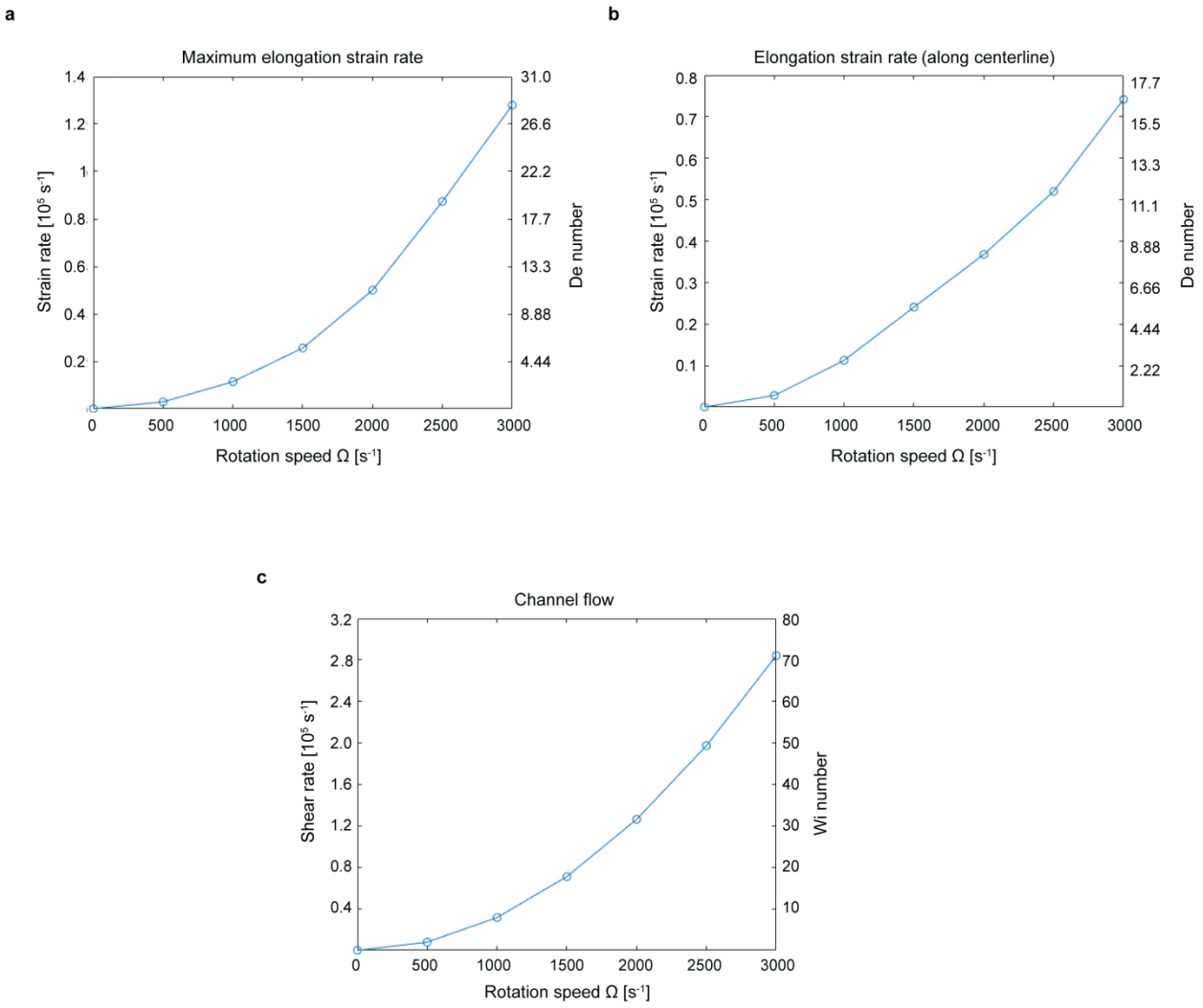

Fig. S8 Deborah (De) and Weissenberg (Wi) numbers for different rotation speeds by CFD simulations. (**a**) Maximum elongation strain rates and corresponding De numbers calculated for specific rotation speeds (0 – 3,000 s^{-1}) of the RJS reservoir. Results show an increase of De number with increasing rotation speeds. For the maximum rotation speed of 3,000 s^{-1}, a strain rate of $\mathbf{1.3 \times 10^5}$ s^{-1} and De number of 28.9 were calculated. (b) Elongation strain rates and corresponding De numbers along the centerline calculated for specific rotation speeds. For the maximum rotation speed, a strain rate of $\mathbf{0.76 \times 10^5}$ s^{-1} and De number of 16.6 were calculated. (c) Shear strain rates and corresponding Wi number calculated for different rotation speeds. For the maximum rotation speed, a shear rate of $\mathbf{2.9 \times 10^5}$ s^{-1} and Wi number of 79.0 were calculated.

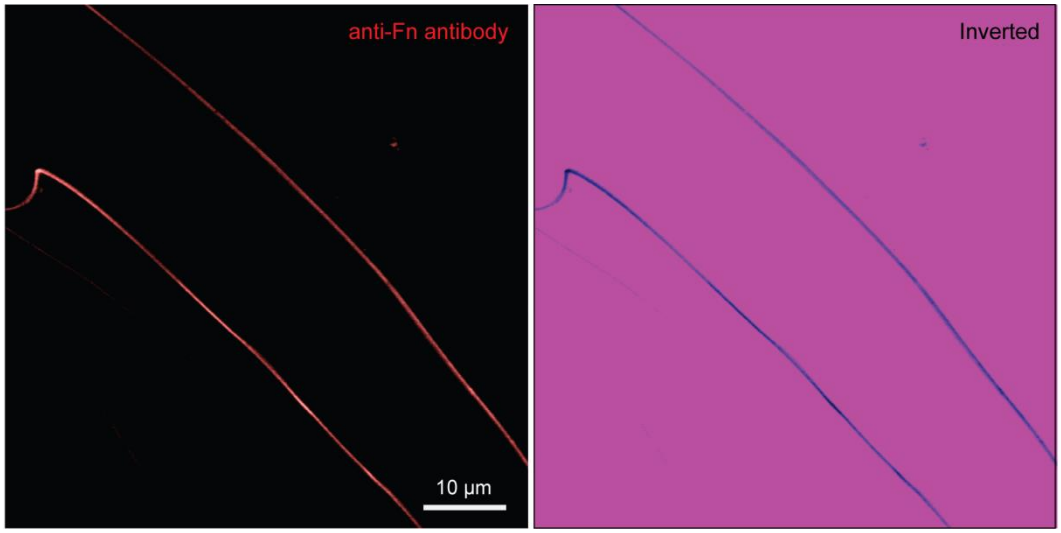

Fig. S9 Immunostained Fn fibers. Image of two Fn nanofibers stained with a anti-human Fn antibody confirms molecular integrity of Fn post-spinning.

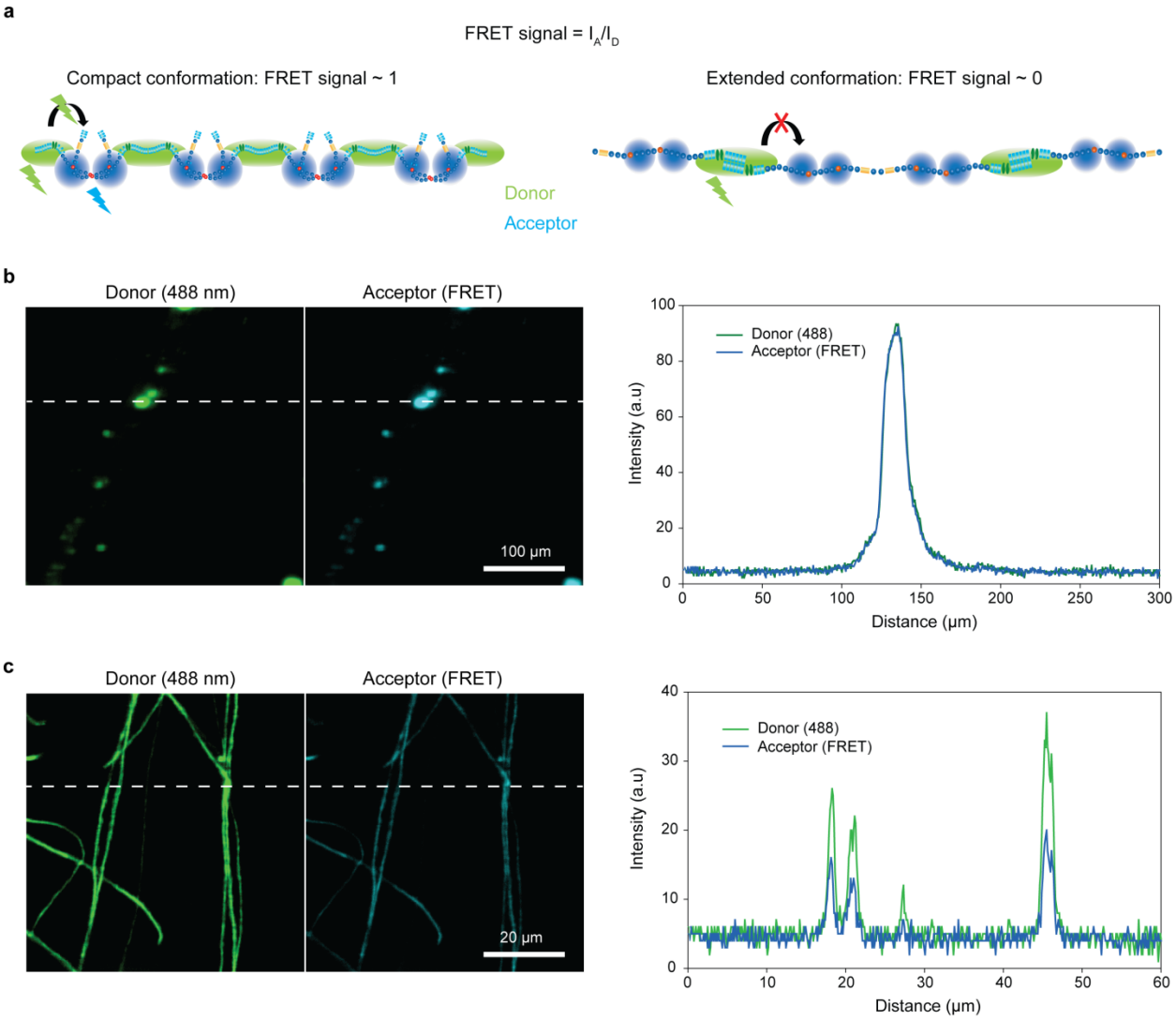

Fig. S10 Conformational structure of Fn nanofibers by FRET analysis. (**a**) Schematic of FRET fluorescence, with a high FRET signal (close to 1) for the compact globular conformation and low FRET signal (close to 0) for the fully extended fibrillar conformation. (**b**) Confocal images at donor emission wavelength (520 nm) and acceptor emission wavelength (576 nm) were taken using the donor excitation wavelength (488 nm). Dual-labeled globular Fn adsorbed on glass coverslips shows strong FRET signal (compact conformation). (**c**) Dual-labeled Fn unfolded using the RJS shows a weak FRET signal (fibrillar conformation). Confocal images are also shown**.**

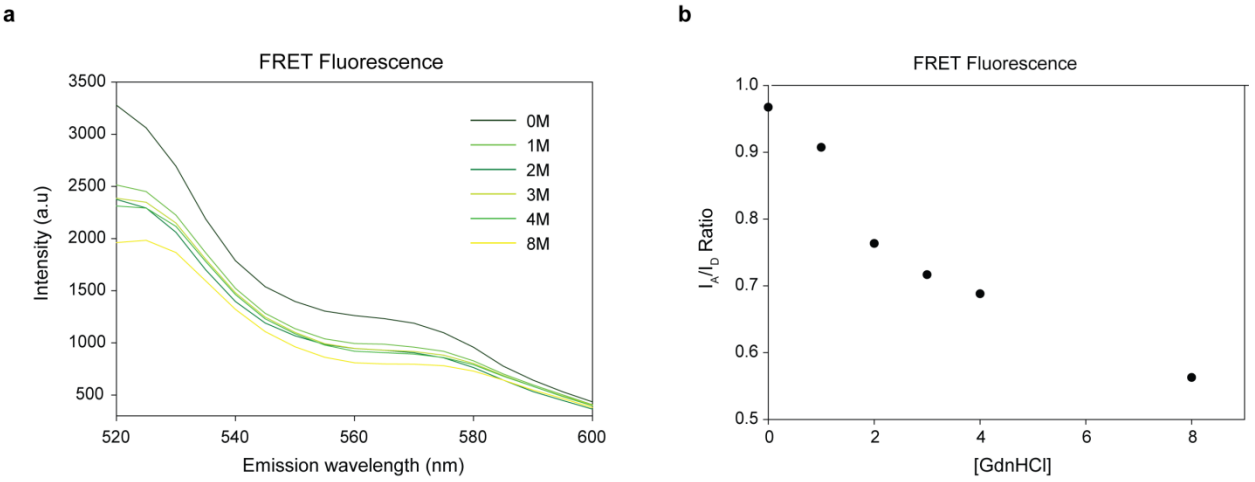

Fig. S11 FRET sensitivity calibration for Fn unfolded via GdnHCl. (**a**) FRET fluorescence spectra of labeled Fn in solution, measured for increasing concentration of [GdnHCl]. FRET signal decreases with increasing concentration of [GdnHCl]. (**b**) The acceptor intensity (IA) and the donor intensity (ID) ratios (IA/ID) were calculated to show sensitivity of FRET measurements of Fn unfolding. FRET was lowest for exposure to 4M and 8M of [GdnHCl] with FRET signals of 0.688 and 0.5626, respectively.

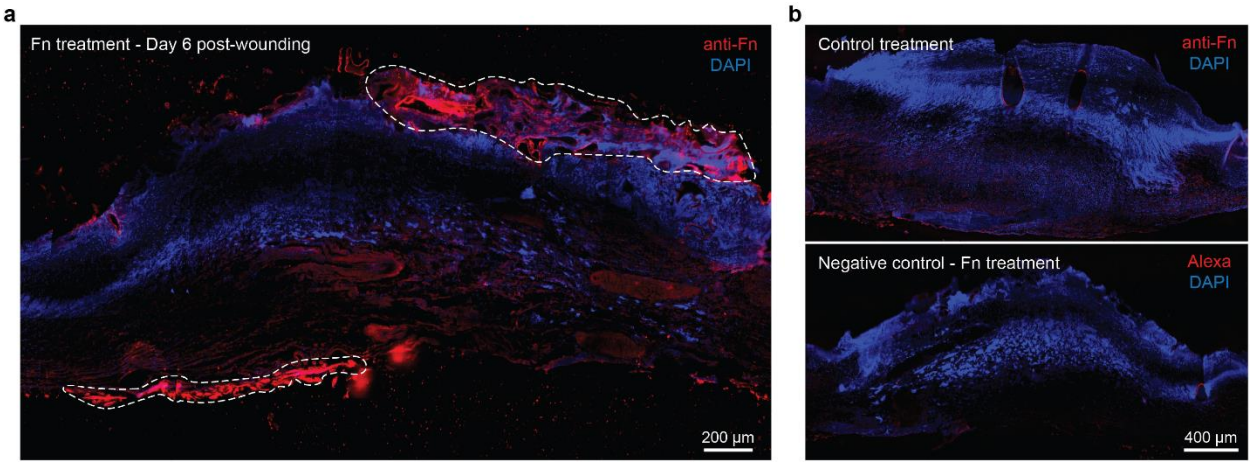

Fig. S12 Fn biodegradation confirmed 6 days post-wounding. (**a**) Fn-treated wounded tissue immunostained with an anti-Fn antibody (red) and DAPI (blue), depicting the presence of low amounts of Fn fibers in the reforming tissue. (**b**) Control immunostaining at day 6 on the non-treated control wound (top) and negative control staining without primary anti-Fn antibody (bottom).

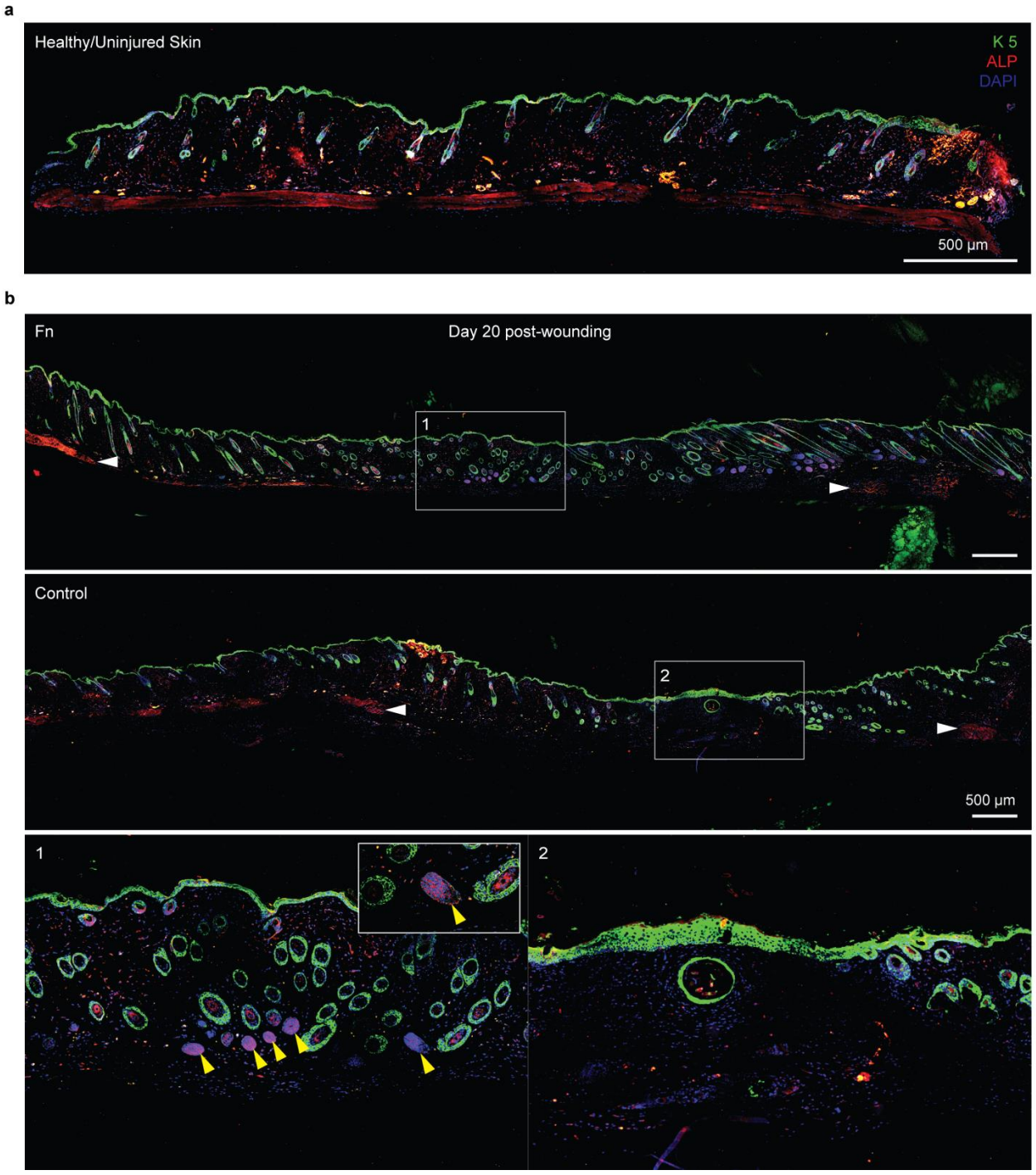

Fig. S13 Fn nanofibers supported recruitment of dermal papillae and epithelial cells throughout wounded tissue. (**a**) Healthy tissue section stained for Alkaline Phosphatase (ALP), Keratin 5 (K5) and DAPI confirmed the presence of DPs and ECs. (**b**) Further histochemical stains of tissues treated with Fn nanofiber wound dressings and the control 20 days post injury. White arrowheads indicate original wound edges. Yellow arrowheads in Fn-treated skin tissue highlight the presence of ALP-positive cell niches, suggesting the presence of dermal papillae (Inset 1). Images reveal decreased density and distribution of ALP and K5-positive cells in the control, which is significant at the wound center (Inset 2).

SI Movies

Movie S1 Close-up movie (time x 4) of the fabrication of Fn nanofibers using a RJS setup. Fn solution is extruded in the rotating reservoir using a 1 mL pipette. Fibers were collected on a mandrel post spinning.

Movie S2 Brightfield microscope movie (real-time) of a Fn nanofiber placed in water and subsequently removed from water.

Movie S3 Differential interference contrast time-lapse movie (time x 50) of a single Fn nanofiber under uniaxial tensile testing (~300 strain).